2D Materials

Superposition of intra- and inter-layer excitons in twistronic $MoSe_2/WSe_2$ bilayers probed by resonant Raman scattering

To cite this article before publication: Liam McDonnell *et al* 2021 *2D Mater.* in press https://doi.org/10.1088/2053-1583/abe778

Superposition of intra- and inter-layer excitons in twistronic $MoSe_2/WSe_2$ bilayers probed by resonant Raman scattering

Liam P. McDonnell[1], Jacob J.S. Viner[1], David A. Ruiz-Tijerina[2], Pasqual Rivera[3], Xiaodong Xu[3], Vladimir I. Fal'ko[4,5] and David C. Smith[1]*

[1] School of Physics and Astronomy, University of Southampton, Southampton SO17 1BJ, United Kingdom.

[2] Centro de Nanociencias y Nanotecnología, Universidad Nacional Autónoma de México, C.P. 22800, Ensenada, Baja California, México.

[3]Department of Physics, University of Washington, Seattle, WA, USA.

[4]National Graphene Institute, University of Manchester, M13 9PL, United Kingdom.

[5] Henry Royce Institute for Advanced Materials, University of Manchester, Manchester, M13 9PL, United Kingdom.

*Corresponding author – D.C.Smith@soton.ac.uk

Hybridisation of electronic bands of two-dimensional materials, assembled into twistronic heterostructures, enables one to tune their optoelectronic properties by selecting conditions for resonant interlayer hybridisation. Resonant interlayer hybridisation qualitatively modifies the excitons in such heterostructures, transforming these optically active modes into superposition states of interlayer and intralayer excitons. For $MoSe_2/WSe_2$ heterostructures, strong hybridization of both single particle and excitonic states can occur via single particle tunneling. Here we use resonance Raman scattering to provide direct evidence for the hybridisation of excitons in twistronic $MoSe_2/WSe_2$ structures, by observing scattering of specific excitons by phonons in both WSe_2 and $MoSe_2$. We also demonstrate that resonance Raman scattering spectroscopy opens up a wide range of possibilities for quantifying the layer composition of the superposition states of the exciton and the interlayer hybridisation parameters in heterostructures of two-dimensional materials.

Monolayers of transition-metal dichalcogenides (TMD) are semiconductors with a plethora of appealing optical properties [1–3]. Unlike the bulk compounds, they feature a direct band gap and a strong light-matter interaction involving optical transitions between the K-valleys electrons and holes [4,5]. Angular momentum, implicit in the conduction and valence band K-valleys states that are dominated by transition metal d-orbitals, determines a valley-selective coupling to the circularly polarised light. At the same time, spin-orbit coupling in transition-metals sets a tight spin-valley locking for the valence band holes, leading to the spin-selectivity of the optical transitions in each valley[2].

In van der Waals heterostructures of TMDs [8], these properties are additionally enriched by the layer-indirect optical transitions[9] across the type-II interface. These excitations are much more sensitive to twist angle than the intralayer excitons. Changing between parallel ($\theta \approx 0^o$) and anti-parallel layer ($\theta \approx 60^o$) alignment changes the energy of bright interlayer excitons by the spin-orbit splitting of carrier in the 'rotated' layer (see Fig 1). Also, for twist angles near (anti)parallel alignment, a twist-dependent momentum mismatch between K-valleys means that optically active interlayer excitons (IX) have a finite centre of mass momentum and substantial kinetic energy creating the conditions for valley memory[9], tunability of the lifetime, accumulation of high densities of IX, and even Bose-Einstein condensation[10] at low temperatures.

Interlayer tunnelling of electrons and holes also leads to the hybridisation of the intralayer and interlayer excitons (see Fig 1). This can lead to strong hybridisation when energies of the two states are resonant [8]. Such resonant conditions naturally occur in homobilayers and few-layer films of TMDs [9,10]. For some heterostructures, such as highly aligned $MoSe_2/WS_2$ bilayers, strong hybridisation has been observed[11] between the nearly degenerate lowest-energy IX and the $MoSe_2$ A exciton, due to the nearly degenerate conduction band edges in the two layers and similar binding energies for the two exciton species. Evidence for the resonance anti-crossing due to the interlayer hybridisation of excitons has also been found in reflectivity spectra of both WS_2/MoS_2 and $MoSe_2/WSe_2$ bilayers[12], which involved the B exciton in WX_2 and a layer-indirect exciton IX with electron on the tungsten and hole on the molybdenum layer. Here, we employ resonance Raman scattering (complemented by reflectivity and photoluminescence spectroscopy, all at 4 K) both to identify the anti-crossing features related to the IX*

and B excitons hybridization in $WSe_2/MoSe_2$ heterobilayers and to determine the layer composition of the superposition states of these excitons, together with the value of the interlayer coupling.

Raman scattering has a unique ability to determine the nature of the phonons responsible for scattering specific optically active electronic excitations, e.g. excitons. In addition, resonant enhancement of the Raman scattering when the incoming or outgoing photon energies coincide with specific exciton states means that resonance Raman scattering studies (rRs) permit us to access the same information on the exciton energies and linewidths as optical absorption and photoluminescence measurements. By observing the resonance behaviour of phonons due to both the WSe_2 and $MoSe_2$ monolayers[13,14] at hybridised excitons[8] in heterostructures one can directly quantify the exciton's layer composition. Below, we report the results of such studies performed on several $MoSe_2/WSe_2$ heterobilayers. These include sample HS1, where anti-parallel alignment of the 2D crystals (at θ=57°) promotes the inter-intralayer exciton hybridization, and a reference sample HS2 (θ=20°), where no interlayer hybridisation is expected due to a large momentum mismatch of the band edges in the two layers (additional samples with θ=6° and θ=60° are discussed in the supplementary information (SI)). The rRs data in this paper focuses on excitation photon energies from 2.05 eV to 2.27 eV and is part of a larger dataset containing data for energies from 1.6 to 2.27 eV. This allows us to probe the excitonic resonances A1s, A2s, B1s and B2s in $MoSe_2$ and A1s, A2s and B1s and WSe_2 (A1s and B1s are the ground-state excitons in the two spin-orbit-split bands, and A2s and B2s are their first optically active excited states). To remove unwanted, luminescence from the rRs spectra the sample was excited with a linearly polarised excitation and Raman scattered light measured for both parallel and crossed polarisations, allowing unpolarised luminescence to be removed (see methods for more detail).

In Fig 2a we present Raman spectra for monolayers of WSe_2 and $MoSe_2$ when resonant with their respective A1s excitons along with Raman spectra for HS1 and HS2 measured in resonance with the WSe_2 intralayer A1s exciton. As expected, the Raman spectra for HS1 and HS2 are almost identical to the WSe_2 monolayer spectra with only minor variations in the relative intensity of different peaks. In Fig 2b we present Raman spectra for both monolayers and heterostructures taken with an excitation photon energy of 2.161 eV, which is near resonance with the WSe_2 B1s exciton. At this excitation

energy, in sample HS1, we observe three new peaks at 291, 309 and 354 cm^{-1} which do not appear in the other samples or at other resonances of HS1. In addition, in HS1 there is a peak at 241 cm^{-1}, which is anomalously strong (~ 3 times greater than in monolayer WSe_2 and HS2). The resonance Raman data in Fig 3 also demonstrates the unique behaviour of these new Raman peaks. For monolayer WSe_2 (Fig 3a) all of the Raman peaks appear to have a broad resonance centred at ~ 2.180 eV. Likewise in HS2 (Fig 3c) all the peaks demonstrate a broad resonance centred at ~2.170 eV. In contrast in HS1 (Fig 3b) the WSe_2 peaks at 257, 261 and 396 cm^{-1} have a resonance centred at ~ 2.18, whereas the new peaks at 241, 291, 309 and 354 cm^{-1} have a resonance which peaks at a lower energy ~2.15 eV and is narrower. As a result in HS1 it is clear that the four new peaks have a common resonance behaviour which is different from the other peaks observed in HS1 or the other samples. Based upon Raman spectra reported for few layer WSe_2 and $MoSe_2$ [15,16], along with spectra for heterobilayers containing either $MoSe_2$ or WSe_2 layers[17–20] we assign the peaks at 309 and 354 cm^{-1} to the WSe_2 and $MoSe_2$ $A_2''(\Gamma)$ phonons. Based upon the assignment of a $MoSe_2$ phonon we also assign the peak at 291 cm^{-1} to the $MoSe_2$ $E'(\Gamma)$ phonon and the peak at 241 cm^{-1} to the $MoSe_2$ $A_1'(\Gamma)$. Both of which are observed at the same shift in the monolayer and heterostructure samples when resonantly exciting the $MoSe_2$ A1s and B1s excitons.

Whilst the observation of three $MoSe_2$ phonons at energies far from $MoSe_2$ resonances and near a predominantly WSe_2 B1s resonance is quite unexpected, it can be explained if the rRs probes an exciton which is a superposition of two excitons which involves electron/hole states in both the WSe_2 and $MoSe_2$ layers. We can also discard the possibility that these new peaks are hybridised phonon modes[17] as they are not observed at any of the other resonances. While the observed Raman scattering at $MoSe_2$ A1s and B1s and WSe_2 A1s resonances are only weakly perturbed by the other layer in the heterostructures, the WSe_2 B1s state is significantly hybridised with an exciton involving electrons in the $MoSe_2$ layer which excites $MoSe_2$ phonons, leading to the observation of peaks in the Raman spectra due to three of the four zone-centre $MoSe_2$ phonons. The fourth zone-centre phonon, the $E''(\Gamma)$, is not observed in any spectra as it is forbidden by an in-plane symmetry which is likely inherited by the heterostructure[16,21].

With clear evidence for exciton hybridisation, we now determine the composition of the hybrid states. Without any $MoSe_2$ intralayer exciton near the WSe_2 B1s energy (see SI), the only other option is its hybridisation with an interlayer exciton. The energy of the fundamental interlayer exciton (IX), in which the electron is in $MoSe_2$ and the hole in WSe_2, is known[14,22] to have an energy of ~ 1.33 eV, and so we can discount it as the hybridised interlayer exciton. However, a higher-energy interlayer exciton (IX^*), which involves an electron in the WSe_2 layer and a hole in $MoSe_2$ layer (see Fig 1a) may have sufficient energy to hybridise resonantly with the B1s in WSe_2 via spin-conserving interlayer tunnelling of a hole. Using a combination of measured transition energies for HS1, experimental lattice and band structure parameters [23–27], and theoretical predictions for monolayer dielectric constants, interlayer band alignment and exciton binding energies [1,28–31](see Methods), we conclude that the energy difference $E_{B1s} - E_{IX^*}$ between the WSe_2 B1s exciton and IX^* is in the range from -17 to 233 meV for a twist angle of 57˚, suggesting that hybridisation of these two states is possible.

Additional information, supporting the hybridisation of the B1s and IX^* excitons to form our hybridised upper (hX_+) and lower (hX_-) excitons, comes from the fine structure of the rRs profiles of the Raman peaks measured in HS1, HS2 and the WSe_2 monolayer (see Fig 4 and SI). Analysis of these profiles using standard third order perturbation theory allows the energies of the excitonic states to be determined. The resonance behaviours of the monolayer and HS2 peaks are dominated by a single (Fig 4a) at 2.156 ± 0.003 eV and 2.161 ± 0.006 eV respectively; the energies and errors were obtained from fitting (see SI). However, HS1 has clear evidence for two hybridised excitonic states in the same energy range, at 2.102 ± 0.001 eV and 2.168 ± 0.001 eV (Fig 4a). In HS1 the peaks also observed in WSe_2 monolayer show two peaks in the rRs profiles, one centred on the energy of each hybridised states (Fig 4a). However, the hybridisation specific peaks at 291, 309 and 354 cm^{-1} show a single narrower resonance between the two energies (Fig 4b). This behaviour occurs because for these phonons scattering between the two hybridised excitons is stronger than scattering within each exciton band [32].

As observed in both the resonance Raman and reflectivity spectra (see Fig 5), the lower energy hybridised state has a significantly lower oscillator strength I_- than the upper's I_+, by a factor of $I_+/I_- \approx 11$ (see SI for more info). As the oscillator strength of the non-hybridised interlayer exciton is

negligible compared to the intralayer exciton, the oscillator strength ratio is a direct measurement of the intralayer exciton component of the two hybridised states (for details, see Methods and the SI). Let ε_{B1s} and ε_{IX^*} be the energies of the non-hybridised B and interlayer excitons, respectively. The hybridised exciton energies are given by

$$\varepsilon_{\pm} = \left(\frac{\varepsilon_{B1s} + \varepsilon_{IX^*}}{2}\right) \pm \sqrt{T^2 + \left(\frac{\varepsilon_{B1s} - \varepsilon_{IX^*}}{2}\right)^2}.$$

Here, T is the mixing energy between the two excitons, related to the interlayer valence-band tunnelling energy t_v as [8]

$$T = \frac{4\sqrt{3}\, t_v}{a_{B1s} a_{IX^*}} \left(\frac{a_{B1s} + a_{IX^*}}{a_{B1s}\, a_{IX^*}}\right) \left[\left(\frac{a_{B1s} + a_{IX^*}}{a_{B1s}\, a_{IX^*}}\right)^2 + \frac{m_e^2 \Delta K^2}{m_{B1s}}\right]^{-\frac{3}{2}},$$

where a_{B1s} and a_{IX^*} are the corresponding exciton Bohr radii, m_e is the mass of the electron shared by both excitons, m_{B1s} the total mass of the WSe_2 B1s exciton, and $\Delta K = 0.066$ Å^{-1} is the mismatch in wavevector between the $MoSe_2$ K' and WSe_2 K valleys for a 57° twist angle.

The ratio between the intralayer exciton components of the hybridised states takes the simple form $I_+/I_- = |\langle \varepsilon_{B1s} | \varepsilon_+ \rangle|^2 / |\langle \varepsilon_{B1s} | \varepsilon_- \rangle|^2 = (\varepsilon_+ - \frac{\varepsilon_{B1s} - \varepsilon_{IX^*}}{2}) / (\varepsilon_+ + \frac{\varepsilon_{B1s} - \varepsilon_{IX^*}}{2})$, which depends indirectly on T. Then, fixing $\varepsilon_{\pm}$ to their corresponding experimental values, 2.102 eV and 2.168 eV, and requiring an oscillator strength ratio of $I_+/I_- = 11$ we obtain $T = 15$ meV and the energies of the non-hybridised B and interlayer excitons as 2.156 eV (in agreement with the monolayer B1s exciton) and 2.110 eV, respectively. This, together with experimental values for the masses[26,27] and Bohr radii obtained from our own solutions to the excitons' Wannier equations (see SI) give the valence-band tunnel coupling as $t_v \approx 11$ meV. The above process is shown in Fig. 6a and b.

Besides providing direct experimental evidence for the hybridisation of layer-direct and -indirect excitons, resonant Raman scattering analysis of intra-layer phonons provides a method for a non-invasive measurement of the interlayer tunnelling for the spin and valley matching states in the crystallographically aligned layers. Obtaining quantitative information on the interlayer hybridisation

constants for the states in heterostructures of two-dimensional semiconductors opens new opportunities for the intelligent design of heterostructures for optoelectronics applications in the areas of quantum technologies. The hybridised layer-direct and -indirect excitons represent a two-level system, which is tunable by an externally applied vertical displacement field [8], and where the superposition of two modes can be operated as an optical qubit. Placing such bilayers inside an optical cavity with a localised photon mode close to the hybridised exciton pair [10,33–35] may additionally open ways towards making a three-level quantum-optical bit for ultra-fast information processing.

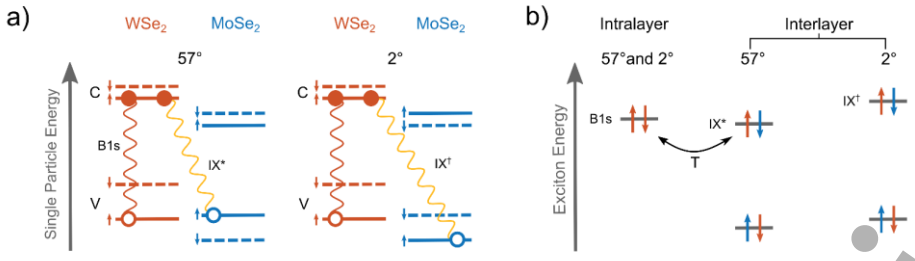

Figure 1 - Energy level diagrams for some of the key single-particle and excitonic states in twisted $MoSe_2/WSe_2$ heterobilayers. a) The level diagrams for the spin-orbit split conduction and valence bands at the WSe_2 K point and the $MoSe_2$ valleys with which they couple in the 57 ° and 2 ° twist heterobilayers. The K points of the layers are defined as the valley in which the highest energy valence band is spin down. The spins, represented by arrows, are the electron spins for both conduction and valence bands in line with the single particle band structure. The spin ordering of the $MoSe_2$ layer changes depending on twist angle due to alignment of either the K′ (57 °) or K (2 °) valleys of the $MoSe_2$ layer with the WSe_2 K valley. The single-particle states which form the WSe_2 B1s intralayer exciton and the interlayer exciton by hole tunnelling, IX* and $IX^{\dagger}$, are joined by wiggly arrows. Single particle tunnelling can couple states for the same carrier (electron or hole), with the same spin and in-plane wavevector in different layers. **b)** Energy level diagram showing the WSe_2 B1s intralayer exciton and the interlayer excitons with which it can couple via single particle tunnelling. For each exciton, the first arrow in each pair represents the electron state (spin and band) and the second arrow indicates the hole state (opposite spin to the empty electron state). The colour of the arrows represents the material in which the carrier resides (WSe_2 orange and $MoSe_2$ blue). The arrow labelled T represents a tunnel coupling between the excitons. As the binding energies of different excitons can differ, the excitonic energies cannot be calculated solely from the single-particle states shown in **a)**. Note that the energy scale for excitons is zoomed in relative to the single particle energy scale.

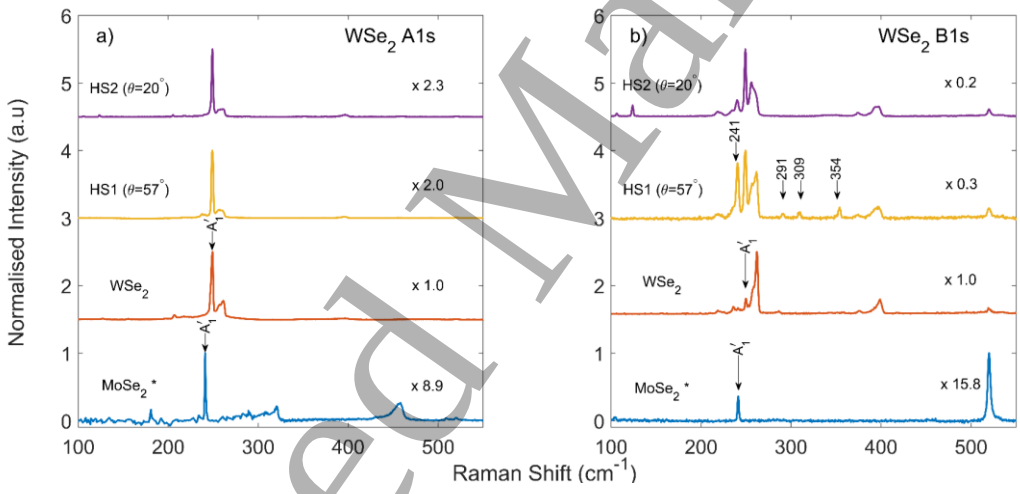

Figure 2 - Resonant Raman scattering spectra of monolayer WSe_2, $MoSe_2$, and their heterostructures (HS). a) Raman spectra for monolayer WSe_2, HS1 (57º) and HS2 (20º) when resonant with the WSe_2 A1s exciton and a spectra for a monolayer $MoSe_2$ when resonant with the $MoSe_2$ A1s exciton. **b)** Raman spectra for an excitation energy 2.161 eV near resonance with the WSe_2 B1s exciton. To allow for ease of visual comparison each spectra has been normalised to the maximum intensity and offset. The scaling factors shown in each panel are relative to the absolute scattering probability of the WSe_2 A_1' peak. In panel **b)** the arrows highlight the new peaks at 241, 291, 309 and 354 cm^{-1}. Unwanted luminescence was removed by subtraction of parallel and perpendicularly polarised Raman spectra (see methods for details).

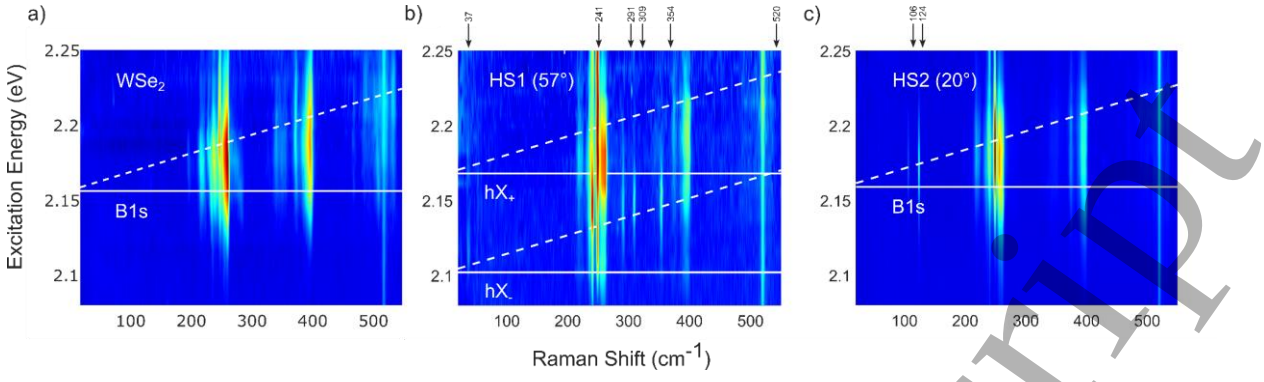

Figure 3 - Comparison of Raman intensity plots between monolayer and heterostructures. Resonance Raman spectra for **a**) monolayer WSe_2, **b**) HS1 (57°), and **c)**, HS2 (20°) are presented for excitation energies from 2.05 to 2.25 eV. The data is plotted using a logarithmic scale for the intensity in order to highlight weak features. Arrows included along the top of panels b) & c) indicate the position of the new peaks in HS1 (241, 291, 309 and 354 cm^{-1}), two defect activated peaks in HS2 106 and 124 cm^{-1}, along with the Si Raman peak at 520 cm^{-1}. The peak at 37 cm^{-1} in HS1 is attributed to a moire zone-folded acoustic phonon like those reported in homobilayers [36,37]. In each colour map the white lines indicate the incoming (solid) and outgoing (dashed) resonance conditions for each excitonic state. For monolayer WSe_2 and HS2 the resonance behaviour is explained in terms of a single resonance with the WSe_2 B1s intralayer exciton. Whereas in HS1 two resonances are required to explain the resonance Raman data. These are attributed to the hybridised excitons formed from the WSe_2 B1s intralayer exciton and interlayer exciton IX* and are labelled as hX_+ and hX_-.

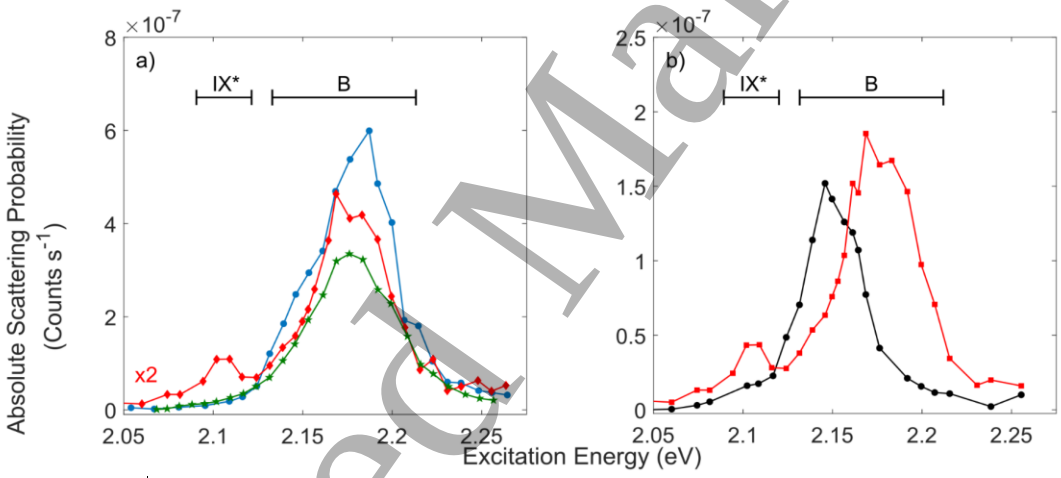

Figure 4 - Resonance Raman profiles for key Raman peaks. a) Resonance profiles for the 257 cm^{-1} peak in the WSe_2 monolayer (blue), HS1 (θ=57°) (red) and HS2 (θ=20°) (green). The 257cm^{-1} peak has potential assignments to the WSe_2 $A_1'(K)$ or $E'(K)$ phonons [13,38] and demonstrates a resonance behaviour which is representative of the other WSe_2 monolayer peaks in HS1. In HS1 the presence of the hybridised interlayer exciton IX* leads to an additional peak in the resonance profile at ~2.1 eV, in addition to the broader resonance associated with the WSe_2 B1s exciton centred at ~ 2.180 eV. **b)** Comparison of the resonance profiles of the 257 cm^{-1} peak, as a representative of the monolayer observed peaks, and 354 cm^{-1}, as a representative of the hybridisation allowed peaks, of HS1. Both the 257 and 354 cm^{-1} resonance profiles can be explained by resonances with both of the hybridised excitons, however, the 354 cm^{-1} profile is centred at a lower energy and appears narrower due to the dominant scattering channel occuring between the two hybridised states. The B exciton/upper hybridised state and the lower hybridised state IX^* regions are marked.

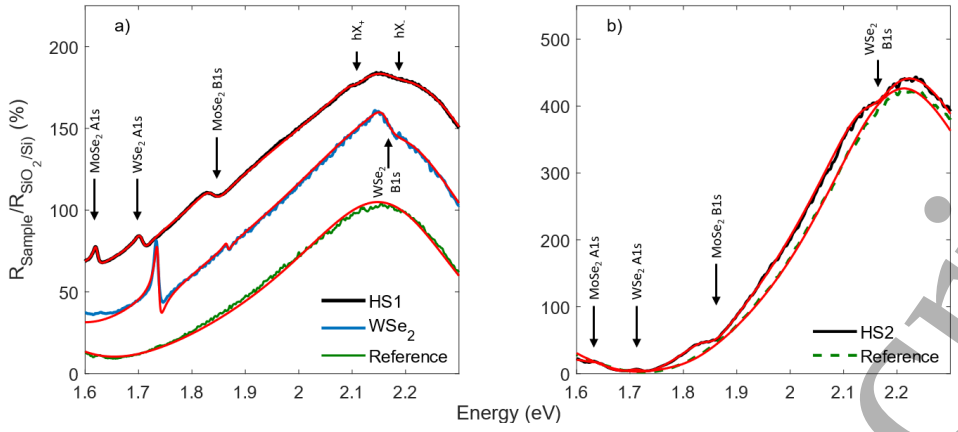

Figure 5 - Reflectivity spectra for both heterobilayer and monolayer regions. The reflectivity spectra measured relative to the SiO_2/Si substrate are presented for **a)** both HS1 and monolayer WSe_2 and **b)** HS2 alongside reference spectra obtained on comparable regions without the TMD layers. In panel a) the reflectivity spectra for monolayer WSe_2 and HS1 have been offset from the reference spectra by 30% and 60% respectively to allow for easier visual comparison. In each case the red lines indicate fits to the reflectivity spectra performed using T-Matrix calculations; the model used to fit the TMD structures differs only from that used for the reference due to the contributions of the TMD layers. The two hybridised states hX_+ and hX_- are clearly visible in the reflectivity for HS1. The oscillator strengths, widths and energies associated with the reflectivity fits are presented in the supplementary information. A complete set of fit parameters is given in the SI and the energies of key transitions are discussed in the main body of the paper.

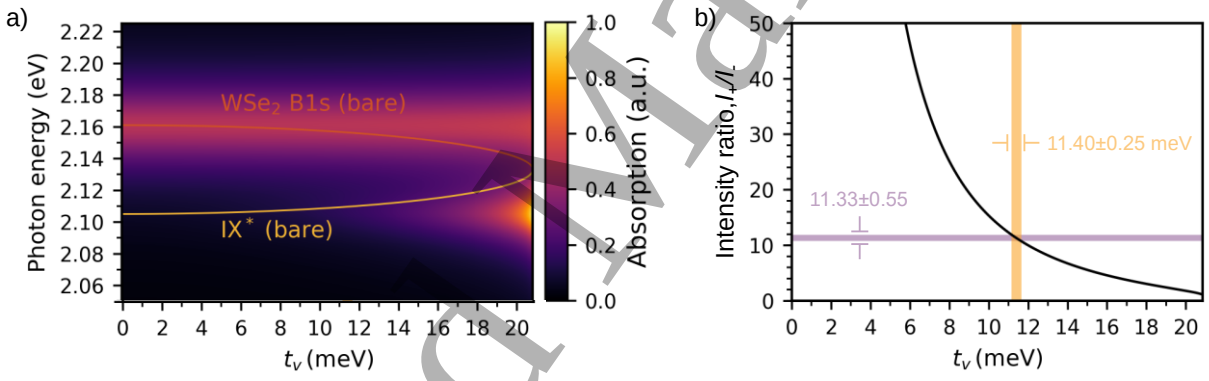

Figure 6 - Twist angle dependent hybridisation of the WSe_2 B1s and IX^* excitons. a) Calculated optical absorption spectrum of hybridized excitons (normalized) for a 57° heterostructure, as a function of the hole tunnelling energy t_v. The bare WSe_2 B1s and IX^* energies corresponding to each value of t_v are shown with solid lines. **b)** Absorption intensity ratio between the higher and lower energy absorption lines. The experimentally measured value is shown in purple and the range of t_v consistent with this measurement is highlighted in yellow. This places the detuning between WSe_2 B1s and IX^* at 46.9 ± 0.4 meV. See Methods for calculation details.

Methods

Experimental Methods

$MoSe_2/WSe_2$ heterobilayers and constituent monolayers were fabricated via mechanical exfoliation and encapsulated in hexagonal boron nitride, using dry stamp transfer [39] on oxide coated silicon substrates. For heterobilayer samples twist angles were determined using optical microscope images and have an uncertainty of ± 1° with the crystal axes of the monolayers determined through second harmonic generation prior to stacking [40]. For all measurements, the samples were held at 4 K in a liquid helium flow cryostat. For the Resonance Raman measurements two laser sources were used a Coherent Mira 900 (1.6 to 1.76 eV) and Coherent CR 599 dye laser (1.74 to 2.27 eV), utilising DCM, Rhodamine 6G and Rhodamine 110 laser dyes. The Raman scattered light was coupled into a Princeton Instruments Tri-vista triple spectrometer equipped with a liquid nitrogen cooled CCD. The samples were excited using a horizontally polarised laser, and the Raman scattered light measured for both parallel and perpendicular linear polarisations. Unwanted luminescence, from the sample, was eliminated by subtraction of the parallel and perpendicular polarised spectra. This allows for removal of unwanted luminescence with negligible effect on the measured Raman intensity due to the strong linear polarisation of the Raman and unpolarised nature of the luminescence signal. Frequency calibration of the Raman spectra was accomplished using the silicon peak at 520 cm^{-1} as an internal reference. Comparison of the Raman intensity across multiple different samples was achieved via an absolute calibration. This involved normalisation to the Silicon Raman intensity, correction for thin film interference effects and use of the absolute Raman cross-section for the silicon peak. Reflectivity spectra were obtained using a Fianium super continuum source and Ocean Optics HR 4000 USB spectrometer, and measured relative to the Silicon substrate. For both Raman and reflectivity measurements the incident power was kept below 100 μW to ensure minimal photo-doping or laser heating of the sample. All optical measurements were performed using a back-scattering geometry with a x50 Olympus objective resulting in a laser spot diameter of ~3 μm on the sample.

For more information on experimental methods and data analysis see supporting information.

Theoretical Model

Estimation of the WSe_2 B1s and interlayer exciton IX^* detuning in anti-parallel stacked $WSe_2/MoSe_2$. To approximate the IX^* energy we solved the Wannier equation for a $MoSe_2$ hole and a WSe_2 electron with effective masses extracted from the earlier publications [23–27] and using the long-range interlayer electron-hole interaction derived in Ref [41]. The layer-indirect gap between $MoSe_2$ valence-band and WSe_2 conduction-band edges (see Fig. 3a), was estimated from the ab initio DFT data reported in Refs. [31,42] and experimental and DFT spin-orbit splitting energies for the $MoSe_2$ valence band and WSe_2 conduction band, respectively [1,27]. Combining this with the exciton binding energy gives a total energy of 2.039 ± 0.111 eV for the momentum-indirect IX^* state, and we estimate an additional kinetic energy of ≈ 17 meV for the bright (momentum-direct) IX^* due to momentum mismatch determined by the interlayer twist angle. Contrasting this with the measured WSe_2 B1s energy of 2.164 ± 0.001 eV we conclude that the detuning between the two excitons is between -17 meV and 233 meV.

Estimation of the interlayer valence-band hopping energy from the resonance Raman spectrum. Hybridization between the intralayer WSe_2 B1s and interlayer IX^* excitons can be modelled by a 4×4 Hamiltonian with one basis state corresponding to WSe_2 B1s, and three representing the valley-mismatched interlayer excitons formed by holes at the three equivalent K valleys of $MoSe_2$, each bound to an electron at the nearest K valley of WSe_2. The intralayer-interlayer exciton hybridization term is related to the interlayer valence-band hopping energy t_v as described in the main text, following Ref. [8]. Diagonalizing the Hamiltonian gives two bright states ψ_- and ψ_+ at energies ε_- and ε_+ with oscillator strengths deriving from their WSe_2 B1s exciton components, and two dark states formed solely by interlayer excitons, which we shall ignore henceforth. We computed the oscillator strength ratio of the two bright states as the modulus squared of the ratio of their WSe_2 B1s components for a range of values of t_v, fixing the energies ε_- and ε_+ at the experimental values for the hybridised exciton resonances, as determined by the rRS data in Fig. 3b. Comparing the theoretical oscillator strength ratios to that

measured by resonance Raman gives a hopping strength $t_v \approx 11$ meV. The available data on the interlayer tunnel coupling for electrons are between 26 and 43 meV [11,12], comparable with our obtained value.

Data Availability

The data presented in this paper is openly available from the University of Southampton Repository at DOI: 10.5258/SOTON.D1314.

Author Contributions

The experiments were conceived by D.C.S, L.P.M and X.X. Samples were fabricated by P.R. The experimental measurements were performed by J.V and L.P.M. Theoretical calculations were performed by D.R.T and V.F. Data analysis and interpretation was carried out by L.P.M, D.C.S, J.V, D.R.T and V.F. The paper was written by D.C.S, L.P.M, D.R.T and V.F. All authors discussed the results and commented on the manuscript.

Corresponding Author

*D.C.Smith@soton.ac.uk

Present Addresses

Competing financial interests

The authors declare no competing financial interests.

Funding Sources

This research was supported by UK Engineering and Physical Sciences Research Council via program grant EP/N035437/1. Both L.P.M and J.V were supported by EPSRC DTP funding. The work at U. Washington was funded by the Department of Energy, Basic Energy Sciences, Materials Sciences and Engineering Division (DE-SC0018171). D.R-T. was funded by UNAM-DGAPA.

References

1. Kormányos, A. *et al.* K · P Theory for Two-Dimensional Transition Metal Dichalcogenide Semiconductors . *2D Mater.* **2**, 022001 (2015).
2. Choi, W. *et al.* Recent development of two-dimensional transition metal dichalcogenides and their applications. *Mater. Today* **20**, 116–130 (2017).
3. Manzeli, S., Ovchinnikov, D., Pasquier, D., Yazyev, O. V & Kis, A. 2D transition metal dichalcogenides. *Nat. Rev. Mater.* **2**, 17033 (2017).
4. Mak, K. F., Lee, C., Hone, J., Shan, J. & Heinz, T. F. Atomically thin MoS_2: A new direct-gap semiconductor. *Phys. Rev. Lett.* **105**, 2–5 (2010).
5. Splendiani, A. *et al.* Emerging photoluminescence in monolayer MoS_2. *Nano Lett.* **10**, 1271–1275 (2010).
6. Yao, W., Xiao, D. & Niu, Q. Valley-dependent optoelectronics from inversion symmetry breaking. *Phys. Rev. B - Condens. Matter Mater. Phys.* **77**, 1–7 (2008).
7. Cao, T. *et al.* Valley-selective circular dichroism of monolayer molybdenum disulphide. *Nat. Commun.* **3**, 887 (2012).
8. Ruiz-Tijerina, D. A. & Fal'Ko, V. I. Interlayer hybridization and moiré superlattice minibands for electrons and excitons in heterobilayers of transition-metal dichalcogenides. *Phys. Rev. B* **99**, 30–32 (2019).
9. Shimazaki, Y. *et al.* Strongly correlated electrons and hybrid excitons in a moiré heterostructure. *Nature* **580**, 472–477 (2020).
10. Król, M. *et al.* Exciton-polaritons in multilayer WSe_2 in a planar microcavity. *2D Mater.* **7**, (2020).
11. Alexeev, E. M. *et al.* Resonantly hybridized excitons in moiré superlattices in van der Waals heterostructures. *Nature* **567**, 81–86 (2019).
12. Hsu, W. T. *et al.* Tailoring excitonic states of van der Waals bilayers through stacking configuration, band alignment, and valley spin. *Sci. Adv.* **5**, 1–7 (2019).
13. McDonnell, L. P., Viner, J. J. S., Rivera, P., Xu, X. & Smith, D. C. Observation of intravalley phonon scattering of 2s excitons in $MoSe_2$ and WSe_2 monolayers. *2D Mater.* **7**, (2020).
14. Seyler, K. L. *et al.* Signatures of moiré-trapped valley excitons in $MoSe_2$ /WSe_2 heterobilayers. *Nature* **567**, 66–70 (2019).
15. Terrones, H. *et al.* New First Order Raman-active Modes in Few Layered Transition Metal Dichalcogenides. *Sci. Rep.* **4**, 1–9 (2014).
16. Soubelet, P., Bruchhausen, A. E., Fainstein, A., Nogajewski, K. & Faugeras, C. Resonance effects in the Raman scattering of monolayer and few-layer $MoSe_2$. *Phys. Rev. B - Condens. Matter Mater. Phys.* **93**, 1–9 (2016).
17. Chiu, M. H. *et al.* Spectroscopic signatures for interlayer coupling in MoS_2-WSe_2 van der waals stacking. *ACS Nano* **8**, 9649–9656 (2014).
18. Wang, K. *et al.* Interlayer Coupling in Twisted WSe_2/WS_2 Bilayer Heterostructures Revealed by Optical Spectroscopy. *ACS Nano* **10**, 6612–6622 (2016).
19. Nayak, P. K. *et al.* Probing Evolution of Twist-Angle-Dependent Interlayer Excitons in $MoSe_2$ /WSe_2 van der Waals Heterostructures. *ACS Nano* **11**, 4041–4050 (2017).
20. Mouri, S. *et al.* Thermal dissociation of inter-layer excitons in MoS_2/$MoSe_2$ hetero-bilayers.

Nanoscale **9**, 6674–6679 (2017).

21. Zhao, W., Ghorannevis, Z. & Kumar, A. K. Lattice dynamics in mono-and few-layer sheets of WS_2 and WSe_2. *Nanoscale* **5**, 9677–9683 (2013).

22. Rivera, P. *et al.* Determination of band offsets, hybridization, and exciton binding in 2D semiconductor heterostructures. *Sci. Adv.* **3**, e1601832 (2017).

23. Wilson, J. A. & Yoffe, A. D. The transition metal dichalcogenides discussion and interpretation of the observed optical, electrical and structural properties. *Adv. Phys.* **18**, 193–335 (1969).

24. Hicks, W. T. Semiconducting Behavior of Substituted Tungsten Diselenide and Its Analogues. *J. Electrochem. Soc.* **111**, 1058 (1964).

25. Al-Hilli, A. A. & Evans, B. L. The preparation and properties of transition metal dichalcogenide single crystals. *J. Cryst. Growth* **15**, 93–101 (1972).

26. Gustafsson, M. V. *et al.* Ambipolar Landau levels and strong band-selective carrier interactions in monolayer WSe2. *Nat. Mater.* **17**, 411–415 (2018).

27. Nguyen, P. V. *et al.* Visualizing electrostatic gating effects in two-dimensional heterostructures. *Nature* **572**, 220–223 (2019).

28. Kumar, A. & Ahluwalia, P. K. Tunable dielectric response of transition metals dichalcogenides MX_2 (M=Mo, W; X=S, Se, Te): Effect of quantum confinement. *Phys. B Condens. Matter* **407**, 4627–4634 (2012).

29. Berkelbach, T. C., Hybertsen, M. S. & Reichman, D. R. Theory of neutral and charged excitons in monolayer transition metal dichalcogenides. *Phys. Rev. B - Condens. Matter Mater. Phys.* **88**, 1–6 (2013).

30. Kang, J., Tongay, S., Zhou, J., Li, J. & Wu, J. Band offsets and heterostructures of two-dimensional semiconductors. *Appl. Phys. Lett.* **102**, (2013).

31. Gong, C. *et al.* Band alignment of two-dimensional transition metal dichalcogenides: Application in tunnel field effect transistors. *Appl. Phys. Lett.* **103**, (2013).

32. McDonnell, L. P., Huang, C.-C., Cui, Q., Hewak, D. W. & Smith, D. C. Probing Excitons, Trions and Dark Excitons in Monolayer WS_2 using Resonance Raman Spectroscopy. *Nano Lett.* **18**, acs.nanolett.7b05184 (2018).

33. Dufferwiel, S. *et al.* Exciton-polaritons in van der Waals heterostructures embedded in tunable microcavities. *Nat. Commun.* **6**, 8579 (2015).

34. Flatten, L. C. *et al.* Room-Temperature exciton-polaritons with two-dimensional WS 2. *Sci. Rep.* **6**, 1–7 (2016).

35. Han, X., Wang, K., Xing, X., Wang, M. & Lu, P. Rabi Splitting in a Plasmonic Nanocavity Coupled to a WS_2 Monolayer at Room Temperature. *ACS Photonics* **5**, 3970–3976 (2018).

36. Lin, M. L. *et al.* Moiré phonons in twisted bilayer MoS_2. *ACS Nano* **12**, 8770–8780 (2018).

37. McDonnell, L. P. *et al.* Experimental realisation of dual periodicity moiré superlattice in a $MoSe_2/WSe_2$ heterobilayer. *arXiv* (2020).

38. De Luca, M. *et al.* New insights in the lattice dynamics of monolayers, bilayers, and trilayers of WSe_2 and unambiguous determination of few-layer-flakes' thickness. *2D Mater.* **7**, (2020).

39. Castellanos-Gomez, A. *et al.* Deterministic transfer of two-dimensional materials by all-dry viscoelastic stamping. *2D Mater.* **1**, (2014).

40. Rivera, P. *et al.* Valley-polarized exciton dynamics in a 2D semiconductor heterostructure. *Science (80-.).* **351**, 688–691 (2016).

41. Danovich, M. *et al.* Localized interlayer complexes in heterobilayer transition metal dichalcogenides. *Phys. Rev. B* **97**, 1–18 (2018).

42. Xu, K. *et al.* The role of Anderson's rule in determining electronic, optical and transport properties of transition metal dichalcogenide heterostructures. *Phys. Chem. Chem. Phys.* **20**, 30351–30364 (2018).